
Comprehensive Analysis of Dewetting Profiles to Quantify Hydrodynamic Slip

Oliver Bäumchen,¹ Renate Fetzner,^{1,2} Andreas Münch,³ Barbara Wagner,⁴ and Karin Jacobs¹

¹ Department of Experimental Physics, Saarland University, D-66123 Saarbrücken, Germany. o.baumchen@physik.uni-saarland.de

² Present address: Ian Wark Research Institute, University of South Australia, Mawson Lakes SA 5095, Australia.

³ School of Mathematical Sciences, University of Nottingham, University Park, Nottingham, NG7 2RD, UK.

⁴ Weierstrass Institute for Applied Analysis and Stochastics (WIAS), Mohrenstrasse 19, D-10117 Berlin, Germany.

Hydrodynamic slip of Newtonian liquids is a new phenomenon, the origin of which is not yet clarified. There are various direct and indirect techniques to measure slippage. Here we describe a method to characterize the influence of slippage on the shape of rims surrounding growing holes in thin polymer films. Atomic force microscopy is used to study the shape of the rim; by analyzing its profile and applying an appropriate lubrication model we are able to determine the slip length for polystyrene films. In the experiments we study polymer films below the entanglement length that dewet from hydrophobized (silanized) surfaces. We show that the slip length at the solid/liquid interface increases with increasing viscosity. The correlation between viscosity and slip length is dependent on the type of silanization. This indicates a link between the molecular mechanism of the interaction of polymer chains and silane molecules under flow conditions that we will discuss in detail.

1 Introduction

1.1 Slippage at Solid/Liquid Interfaces

The control of the flow properties at the solid/liquid interface is important for applications ranging from microfluidics, lab-on-chip devices to polymer melt extrusion. Slippage would, for instance, greatly enhance the throughput in lab-on-chip devices and extruders. Usually slippage is characterized by the so-called slip length which is defined as the distance between the solid/liquid interface and the point within the solid where the velocity profile of the liquid

extrapolates to zero. During the last years, several different techniques have been established to probe the slip length of different systems. These methods can be classified into two groups, direct and indirect measurements of the flow velocity at the solid/liquid interface. Direct measurements are based on particle imaging velocimetry techniques [1, 2, 3] that utilize tracer particles or fluorescence recovery after photobleaching [4, 5]. Colloidal probe atomic force microscopy [6, 7] and surface forces apparatuses [8, 9] are more indirect techniques to probe slippage. Detailed information concerning slippage and techniques to measure liquid velocities in the vicinity of solid/liquid interfaces are reviewed in recent articles by Neto et al. [10], Lauga et al. [11] and Boquet and Barrat [12].

1.2 Dewetting Dynamics of Polymer Films

Dewetting takes place whenever a liquid layer can reduce energy by retracting from the contacting solid [13]. Dewetting starts by the birth of holes, which can be generated by three different mechanisms, spinodal dewetting, homogeneous and heterogeneous nucleation [14]. The holes grow in size, c.f. Fig. 1, until neighboring holes touch. The quasi-final state is a network of droplets [15]. The equilibrium state would be a single droplet, yet this state is usually not awaited since it may take years for viscous liquids such as our polystyrene. Since we are only interested in the growth of holes and their rim morphology, the underlying mechanism of their generation is irrelevant. However, the most likely process in our system is nucleation. The type of nucleus is unclear and also of no relevance for our studies. It can be a dust particle or a heterogeneity in the film or on the substrate. After holes are generated, they instantly start to grow until they touch neighboring holes and coalesce. We study the flow dynamics of thin polymer films on smooth hydrophobic substrates. The driving force for the dewetting process can be characterized by the spreading parameter S , which depends on the surface tension of the liquid γ_{lv} (30.8 mN/m for polystyrene) and the Young's contact angle Θ of the liquid on top of the solid surface:

$$S = \gamma_{lv}(\cos\Theta - 1) \quad (1)$$

The system also dissipates energy, namely by viscous friction within the liquid and sliding friction at the solid/liquid interface. A force balance between driving forces and dissipation determines the dewetting rate. Conservation of mass leads to a rim that surrounds each hole. We show that the shape of this rim is not only sensitive to the chain length of the polymer melt [16] but is also to the underlying substrate. The use of recently developed models [17] enables us to extract the slip length b as well as the capillary number Ca from the rim profiles. The latter is given by

$$Ca = \frac{\eta \dot{s}}{\gamma_{lv}} \quad (2)$$

Here, \dot{s} is the current dewetting velocity, which can be obtained by a series of optical images of the hole growth before the sample is quenched to room temperature and imaged by atomic force microscopy (AFM). From the capillary number, the viscosity η of the melt can be calculated and compared to independent viscosity measurements, cf. Sect. 3.4.

2 Experimental Section

2.1 Our System

Atactic polystyrene (PS) obtained from PSS Mainz with a molecular weight of 13.7 kg/mol ($M_w/M_n = 1.03$) was used as a liquid in our experiments. As substrates, we used Si wafers (Siltronic AG, Burghausen, Germany) that were hydrophobized by two different types of silanes following standard methods [18]. Thin PS films were prepared by spin coating a toluene solution of PS onto mica, floating the films onto Millipore water, and then picking them up with the silanized silicon wafers. The floating step is necessary since on the spin coater, a drop of toluene solution would just roll off the hydrophobized surface. All PS films in this study have a thickness of 130(5) nm. We utilized two different silane coatings on the Si wafer (2.1 nm native oxide layer): octadecyltrichlorosilane (OTS) and the shorter dodecyltrichlorosilane (DTS), respectively. The thicknesses of these self-assembled monolayers are $d_{\text{OTS}} = 2.3(2)$ nm and $d_{\text{DTS}} = 1.5(2)$ nm as determined by ellipsometry (EP³ by Nanofilm, Goettingen, Germany). The contact angle hysteresis of water is very low (6° in case of OTS and 5° in case of DTS), while the advancing contact angles are $116(1)^\circ$ (OTS) and $114(1)^\circ$ (DTS). Surface characterization by AFM (Multimode by Veeco, Santa Barbara, CA, USA) revealed RMS roughnesses of 0.09(1) nm (OTS) and 0.13(2) nm (DTS) on a $1\text{ }\mu\text{m}^2$ area, and an (static) receding contact angle of polystyrene droplets of $67(3)^\circ$ on both substrates.

Surface energies cannot be determined directly from contact angle measurements of PS only, due to the fact that polystyrene has polar contributions. The advancing contact angles of apolar liquids like bicyclohexane vary slightly on both coatings. We find $45(3)^\circ$ on OTS and $38(4)^\circ$ on DTS. The surface energy of the substrate is linked to the contact angle of apolar liquids via the Good-Girifalco equation [19]. Consequently, we find a slightly larger surface energy for DTS ($\gamma_{\text{DTS}} = 26.4\text{ mN/m}$) than for OTS ($\gamma_{\text{OTS}} = 23.9\text{ mN/m}$) substrates. Identical contact angles of PS on both substrates therefore lead to different energies at the OTS/PS and DTS/PS interface due to Young's equation.

2.2 Hole Growth Dynamics

To induce dewetting, the films were heated to different temperatures above the glass transition temperature of the polymer. After a short time circular holes appear and instantly start to grow (see Fig. 1).

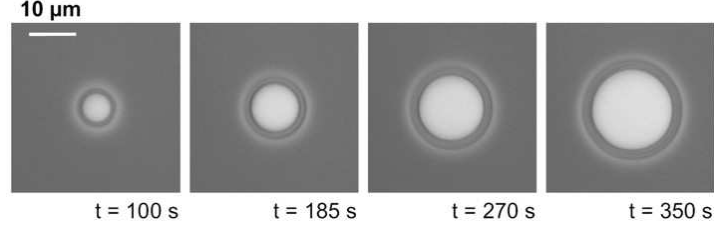


Fig. 1. Series of optical images of a growing hole in a PS film on DTS at 120°C .

Holes in the PS film were imaged by optical microscopy captured by an attached CCD camera, and hole radii were measured. As shown in Fig. 2, dewetting progresses much faster on DTS than on OTS coated substrates.

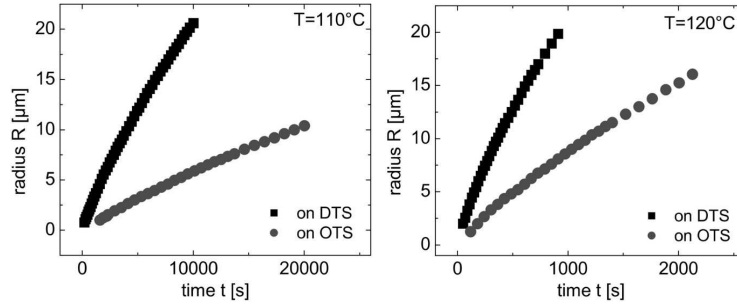


Fig. 2. Hole radius versus time on OTS and DTS at 110°C and 120°C .

We explain these results as follows: At the same temperature, the liquids on both samples have exactly the same properties: the viscosity as well as the surface tension do not depend on the substrate underneath. Additionally, the contact angle of polystyrene on both surfaces is the same within the experimental error. Therefore, the spreading coefficient S , that is the driving force of the dewetting process, is identical on both substrates. Hence, the different dewetting velocities observed on OTS and DTS indicate different energy dissipation pathways on these coatings. Viscous friction within the liquid is expected to be identical for both surfaces since we compare liquids of the same viscosity and with the same dynamic contact angle [20]. The latter can be probed by AFM scans in the vicinity of the three-phase contact line. In

situ imaging reveals that the dynamic contact angle stays constant at $56(2)^\circ$ during hole growth. Consequently, friction at the solid/liquid interface and therefore slippage must be different on OTS and DTS. In the next section we show that not only the hole growth dynamics but also the shape of rims is affected by the underlying substrate.

2.3 Rim Shapes

For the characterization of the shape of the rims surrounding the holes, the samples were quenched to room temperature after the holes have reached a diameter of $12\mu\text{m}$. AFM scans were then taken in the glassy state of PS. An example is shown in Fig. 3.

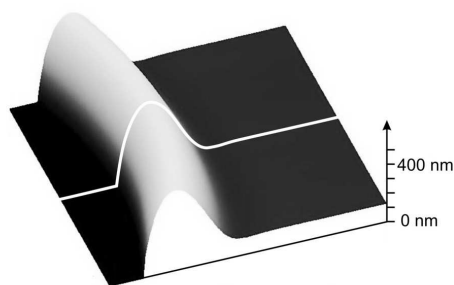


Fig. 3. AFM image of a rim on OTS: scan size $10 \times 10\mu\text{m}^2$. The dewetting was performed at 130°C . The white line represents a single scan line of the rim perpendicular to the three-phase contact line.

Fig. 4 demonstrates that the type of substrate affects the rim profile: On OTS covered substrates, the rim of the dewetting PS film exhibits an oscillatory shape, whereas on DTS covered surfaces, at the same temperature, a monotonically decaying function is observed. The insets to Fig. 4 shall clarify the term "oscillatory rim shape" on OTS. Furthermore, Fig. 4 shows that temperature influences the shape of the profile: the higher the temperature the more pronounced are the oscillations on OTS and even on DTS, an oscillatory shape is recorded for $T = 130^\circ\text{C}$. Comparing the impact of the substrate on the rim morphology to the hole growth experiments in the previous section, we observe a correlation between the dewetting velocity and the shape of corresponding rims: high dewetting velocities lead to monotonic rim profiles while lower dewetting speeds tend to result in oscillatory rim shapes. In the previous section we argued that different sliding friction at the solid/liquid interface might be responsible for the different dewetting speeds on OTS and DTS. In the next section, the theoretical expectation of the influence of slippage on the rim shapes will be explained. Moreover, the experimental results are compared to theoretical predictions.

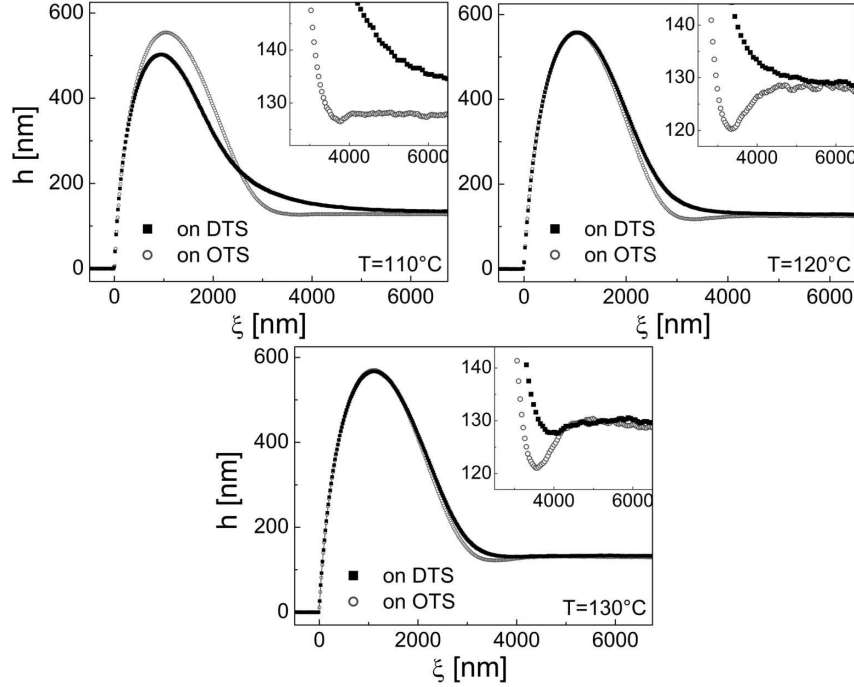


Fig. 4. Rim profiles on OTS and DTS at 110°C, 120°C and 130°C.

3 Theoretical Models and Data Analysis

3.1 Lubrication Model

The theoretical description is based on a lubrication model developed by Münch et al. [21] for systems showing strong slip at the solid/liquid interface. Starting point for this description are the Navier-Stokes equations in two dimensions for a viscous, incompressible Newtonian liquid:

$$-\nabla[p + \phi(h)] + \eta \nabla^2 \mathbf{u} = \rho(\partial_t \mathbf{u} + \mathbf{u} \cdot \nabla \mathbf{u}) \quad \nabla \cdot \mathbf{u} = 0, \quad (3)$$

with pressure p , disjoining pressure $\phi(h)$, viscosity η , density ρ and the velocity $\mathbf{u} = (u, w)$ of the liquid.

By applying the Navier slip boundary condition

$$b = \frac{u}{\partial_z u}|_{z=0} = \frac{\eta}{\kappa}, \quad (4)$$

where η is the viscosity of the melt and κ the friction coefficient at the solid/liquid interface, and using a lubrication approximation (which assumes that the typical length scale on which variations occur is much larger in lateral direction than in vertical direction) we get the following equations of motion:

$$u = \frac{2b}{\eta} \partial_x (2\eta h \partial_x u) + \frac{bh}{\eta} \partial_x (\gamma \partial_x^2 h - \phi'(h)) \quad (5)$$

$$\partial_t h = -\partial_x (hu) \quad (6)$$

Here, the slip length b is assumed to be much larger than the average film thickness H (i.e., for $b/H \gg 1$). In order to perform a linear stability analysis of the flat film of thickness H we introduce a small perturbation $\delta h \ll H$ traveling in the frame of the moving rim

$$h(x, t) = H + \delta h \exp(k\xi) \quad (7)$$

with

$$\xi = x - s(t) \quad (8)$$

where $s(t)$ is the position of the three-phase contact line. This ansatz leads to the characteristic polynomial of third order in k :

$$(Hk)^3 + 4Ca(Hk)^2 - Ca \frac{H}{b} = 0 \quad (9)$$

One of the three solutions for k is real and positive and therefore does not connect the solution to the undisturbed film for large ξ . Hence, this solution is not taken into account any further. The remaining two solutions k_1 and k_2 are either a pair of complex conjugate numbers with negative real part or two real numbers < 0 . These two different sets of solutions correspond to two different morphologies of the moving rim, i.e., either an oscillatory (k_1 and k_2 are complex conjugate) or a monotonically decaying (k_1 and k_2 are real) shape. These morphologies are separated by a distinct transition as indicated by the dashed line in Fig. 5. If both the capillary number Ca and the slip length b are given for a certain film thickness H , it is possible to qualitatively predict the shape of the rim. This is in good agreement with our experimental observations: On DTS we observe fast dewetting and expect large slip lengths, and we indeed observe mainly monotonically decaying rims; on OTS we find slower dewetting and expect comparatively small slip lengths, and, again in agreement with the theoretical prediction, we observe oscillatory profiles.

Furthermore, if two solutions k_1 and k_2 are known (or extracted from experimentally obtained rim profiles), the characteristic polynomial can be solved for the unknown slip length b and the capillary number Ca . By that we obtain the solution for b and for Ca from the strong-slip lubrication model:

$$b_{lub} = \frac{1}{4H} \frac{k_1^2 + k_1 k_2 + k_2^2}{k_1^2 k_2^2} \quad (10)$$

$$Ca_{lub} = -\frac{H}{4} \frac{k_1^2 + k_1 k_2 + k_2^2}{k_1 + k_2} \quad (11)$$

Besides this strong slip model, further lubrication models have been developed [17, 21]. The corresponding weak slip (i.e., for $b/H < 1$) model always leads to complex solutions for k_1 and k_2 and therefore predicts only oscillatory rim shapes.

3.2 Stokes Model

As already mentioned, the former introduced lubrication model is just valid for large slip lengths compared to film thickness. To handle smaller slip lengths it is necessary to use a more recently developed model [17] which is a third-order Taylor expansion of the characteristic equation gained by linear stability analysis of a flat film using the full Stokes equations:

$$\left(1 + \frac{H}{3b}\right)(Hk)^3 + 4Ca\left(1 + \frac{H}{2b}\right)(Hk)^2 - Ca\frac{H}{b} = 0 \quad (12)$$

This equation again predicts a transition between oscillatory and monotonically decaying rims. In Fig. 5, the respective transition line (solid line) is compared to the one of the strong-slip lubrication model (dashed line). As expected, significant deviations between the two models occur for moderate and weak slippage, while good agreement is given for strong slippage. As shown in [17], the transition line for the Taylor expansion is, even for small slip lengths, quite close to the one predicted by the full Stokes equations. Solving (12) for b and Ca leads to additional contributions compared to the strong-slip lubrication model, (10) and (11):

$$b_{Taylor} = \frac{1}{4H} \frac{k_1^2 + k_1k_2 + k_2^2}{k_1^2k_2^2} - \frac{H}{2} \quad (13)$$

$$Ca_{Taylor} = -\frac{H}{4} \frac{k_1^2 + k_1k_2 + k_2^2}{k_1 + k_2} + \frac{H^3}{6} \frac{k_1^2k_2^2}{k_1 + k_2} \quad (14)$$

Note that the slip length obtained from the third-order Taylor expansion of the characteristic equation of the full Stokes model equals the slip length obtained from the strong-slip lubrication model minus a shift of half of the film thickness.

We like to point out that, in contrast to previous publications [22, 23], all data sets presented in the following sections were evaluated by applying the third-order Taylor expanded Stokes model, i.e., (13) and (14). This enables us to exclude deviations that occur from the strong-slip lubrication model, which is not valid for smaller slip lengths.

3.3 Method to Extract Slip Length and Capillary Number

To fit the profile of a rim obtained by AFM we choose data points on the "wet" side of the rim ranging from about 110 % of the film thickness to the

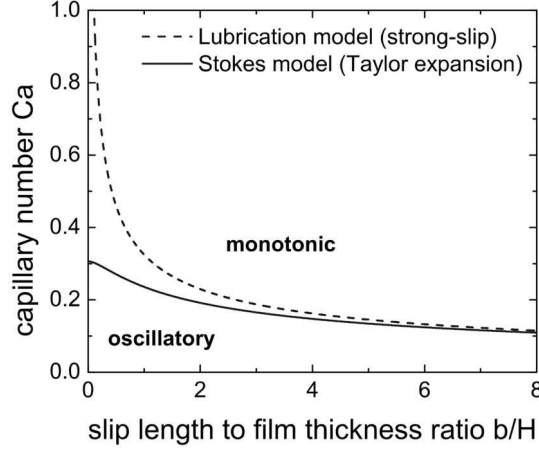


Fig. 5. Comparison of the theoretically expected transition from oscillatory profiles to monotonic ones for the strong-slip lubrication model (dashed line) and the third-order Taylor expanded Stokes model (solid line).

film thickness itself (see Fig. 6). Oscillatory profiles are fitted by a damped oscillation as described by (15) with δh_0 , k_r , k_i and ϕ as fit parameters:

$$\delta h_{osci} = \delta h_0 \exp(k_r \xi) \cos(k_i \xi + \phi) \quad (15)$$

k_r is the real part and k_i the imaginary part of k_1 and k_2 :

$$k_{1,2} = k_r \pm i k_i \quad (16)$$

In case of monotonically decaying rims we deal with a superposition of two exponential decays given by (17):

$$\delta h_{mono} = \delta h_1 \exp(k_1 \xi) + \delta h_2 \exp(k_2 \xi) \quad (17)$$

Here we obtain the amplitudes $\delta h_{1,2}$ and the decay lengths $k_{1,2}$ as fit parameters. In some cases, the fitting procedure may not be able to distinguish between two decaying exponentials, leading to two identical decay lengths. In that case, an independent calculation of b and Ca is not possible. However, if the capillary number Ca is known (for example if the viscosity is known and the capillary number was calculated via (2)), one decay length is sufficient to extract the slip length.

From the parameters k_1 and k_2 gained by fitting the respective function (15) or (17) to the rim profiles, we determined slip lengths via (13) and capillary numbers via (14) for the PS films on our substrates at different temperatures, i.e., for different melt viscosities. As shown in Fig. 7, the capillary number clearly increases non-linearly with the slip length. In the transition region from oscillatory profiles to monotonic decaying rims, we have to deal

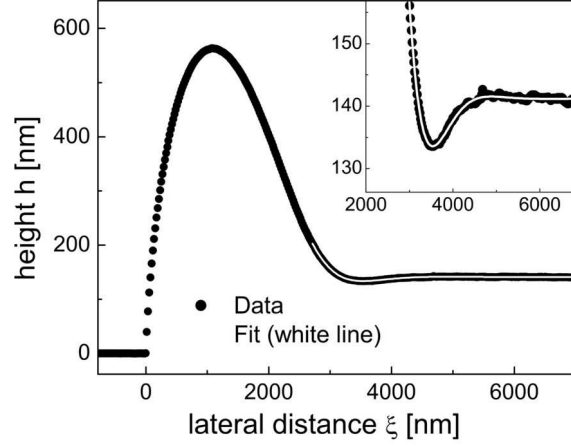


Fig. 6. AFM cross-section of a rim profile of a hole (about $12\mu\text{m}$ radius) in a PS(13.7k) film on OTS dewetted at 120°C and corresponding fit.

with the fact that profiles with just one clear local minimum, but no local maximum in between the minimum and the undisturbed film, can be fitted by (17) as well as by (15). In the first case, this corresponds to one of the amplitudes $\delta h_{1,2}$ being negative. We emphasize that exclusively (15) leads to slip lengths that do not depend on the hole radius R , cf. the recent study [17]. This criterion enables us to justify the choice of (15) as the appropriate fitting function in this region.

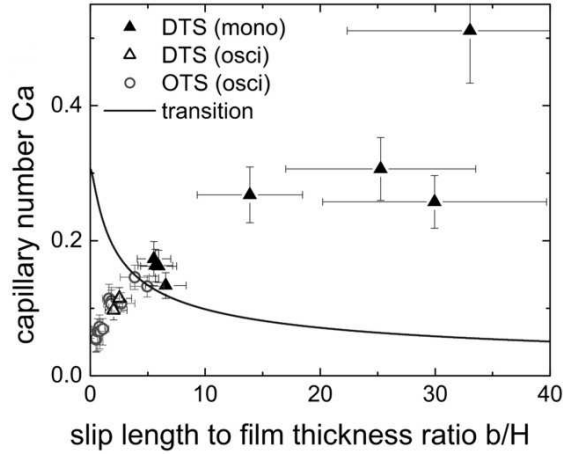


Fig. 7. Capillary number Ca versus the ratio of slip length b and film thickness H on OTS and DTS obtained from the third-order Taylor expanded Stokes model.

3.4 Experimental Tests

The independent extraction of capillary number Ca and slip length b from the rim profiles allows us to check the consistency of the applied model. Comparing for instance the viscosities gained by rim shape analysis (via the calculated capillary numbers, the dewetting velocities \dot{s} from hole growth experiments and (2)) to independent viscosimetry measurements shows excellent agreement for both types of substrates, cf. Fig. 8.

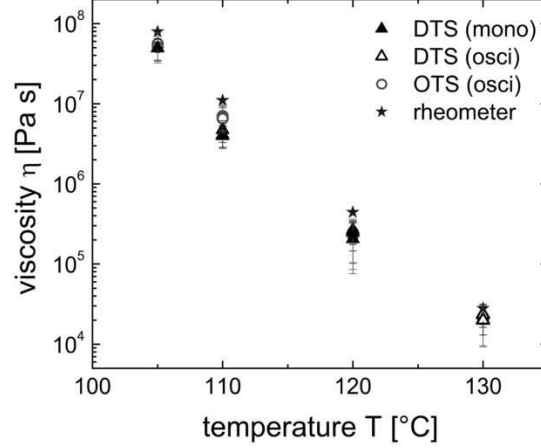


Fig. 8. Viscosities obtained from rim profile analysis and the third-order Taylor expanded Stokes model compared to viscosimetry data.

Furthermore we evaluated certain rim shapes of the same hole but at different hole radii, cf. [23]. Although the rim grows in size during dewetting, the extracted slip length stays constant within the range of our variation of rim size. The extracted capillary number, however, decreases for increasing hole radius. On the other hand, dewetting slows down with increasing rim size, cf. Fig. 2. The ratio of the measured dewetting velocities \dot{s} and the extracted capillary numbers gives viscosity data independent of the hole size, which again is in agreement with the expectation. To conclude, all these tests underline the applicability of the former introduced models to our system.

4 Results and Discussion

Analysis of rim shapes for different temperatures above the glass transition temperature gives slip lengths ranging from less than 100 nm up to about 5 microns.

As shown in Fig. 9, the slip length on DTS is about one order of magnitude larger than on OTS. On both substrates, the slip length decreases for higher

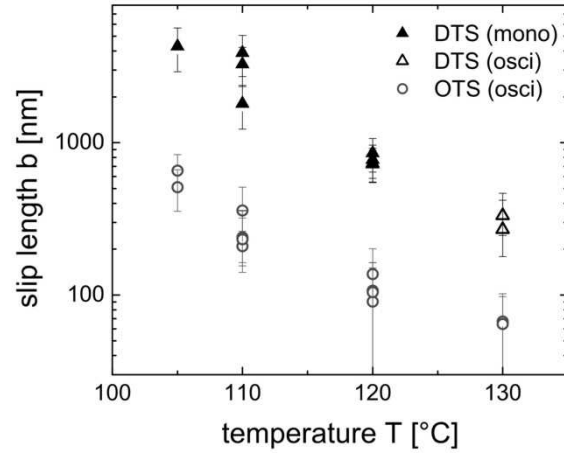


Fig. 9. Slip length b on OTS and DTS versus the dewetting temperature. Rim profile analysis was performed by applying the third-order Taylor expansion of the Stokes model on holes of $12\text{ }\mu\text{m}$ radius in a 130 nm PS(13.7k) film.

temperatures. These results are in good agreement with slip lengths obtained by hole growth analysis studies [24]. Plotting the slip length versus melt viscosity, determined by rim analysis, shows non-linear behavior (see Fig. 10). This is at variance with the Navier slip condition (4), where a linear dependency of slip length on viscosity is expected. To evaluate this discrepancy, experiments were performed with polymer melts of different molecular weights below the entanglement length. The results are shown in Fig. 10. Variation of molecular weight of the melt gives data that fall on a master curve for each substrate. This means that friction has to be stronger for higher viscosities. This fact is possibly a valuable hint to the molecular mechanism of friction and slippage at the solid/liquid interface and will be further discussed in the following.

A scenario described in literature [25, 26, 27] for similar systems concerns melt chains penetrating between silane molecules and adhering to the underlying high-energy silicon substrate. This may lead to polymer chains slipping over grafted polymer chains of the same polymer. For this situation it is reported that flow is expected to be strongly dependent on shear rate and grafting density. The density of adhered chains is assumed to be dependent on the perfectness of the monolayer of the silane molecules. From the surface energies we obtained for OTS and DTS, we might expect OTS to build up a denser layer compared to DTS. Higher shear rates obtained for larger dewetting rates i.e. temperatures may lead to a dynamic desorption of adhered chains and, thus, change friction at the interface. Molecular dynamics simulations of flowing polymer chains interacting with grafted chains of the same polymer by Pastorino et al. [28] have shown that interpenetration and subsequent anchoring

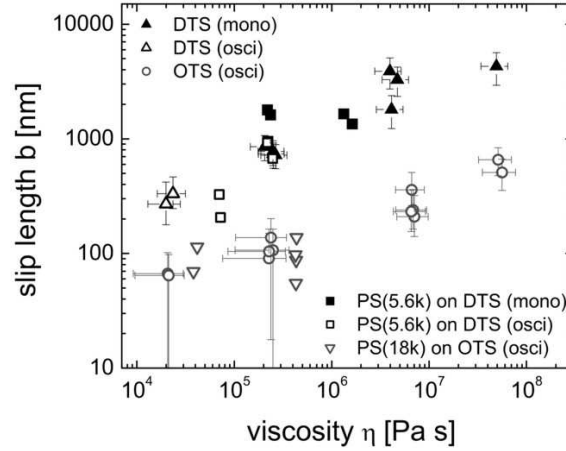


Fig. 10. Slip length data from Fig. 9 versus the respective film viscosity in logarithmic scale.

as well as the grafting density influences slippage. They observe pronounced slippage for lower density of anchored chains.

Our further studies concerning the molecular mechanism of slippage focus on X-ray and neutron reflectivity experiments of (deuterated) polystyrene melts on Si substrates covered with self-assembled monolayers. These techniques are known to be very sensitive on changes at the solid/liquid interface. First X-ray reflectivity measurements on bare silanized wafers show that the silane molecules form very dense monolayers and stand upright on top of the underlying Si substrate [29]. Therefore, the previously discussed explanation of interdigitation does not seem to be very likely. Other explanations assuming structural changes of the substrate, such as bending or tilting of silane molecules, producing a temperature-dependent slip length also seem not to be a major issue in the temperature range of our experiments, though we can not absolutely exclude them. Further, roughness has been shown in miscellaneous studies to influence slippage [27, 30]. However, due to the fact that our surfaces are extremely smooth, cf. Sect. 2.1, the influence of roughness might be safely excluded. Other parameters such as the polarizability of the liquid have been shown to influence slippage dramatically. Cho et al. [31] observed lower slip length for higher polarizable liquid molecules. In addition, the shape of the liquid molecules can also be relevant for differences in slip lengths [5]. Using the same liquid, the latter two aspects can not be responsible for the different slip length on OTS and DTS.

The most probable scenario concerning the origin of the huge slip lengths is the formation of a so-called lubrication layer, i.e., a liquid layer of reduced viscosity close to the substrate, that may build up due to migration of low molecular-weight species to the solid/liquid interface or an alignment of liquid molecules at the interface. This slip plane could cause large apparent slip

lengths. Systematic ellipsometry measurements on spots where a film front has passed the substrate and potentially left a remaining liquid layer, may corroborate this point of view. If lubrication layers are important, then polydispersity of the liquid should play a crucial role on slippage. Dewetting experiments dealing with mixtures or double-layers of polymers with different chain lengths are planned. At last, this argument cannot yet afford explaining the difference in slippage on OTS and DTS of about one order of magnitude. Nevertheless, we can speculate that the formation of this lubrication layer may depend on the interfacial energies of PS and silane brushes, $\gamma_{\text{PS/OTS}}$ and $\gamma_{\text{PS/DTS}}$, which are known to be slightly different, cf. Sect. 2.1.

5 Conclusion

We could show that slippage may strongly affect profiles of moving rims surrounding growing holes in thin liquid films. Furthermore, the connection of fitting parameters concerning the shape of the rims and system parameters as slip length b and capillary number Ca via a theoretical model allows us to quantify slippage. We observe a slip length which is about one order of magnitude larger on DTS than on OTS and which decreases with increasing temperature. Moreover, we record experimentally a non-linear dependency of the viscosity on the slip length, which is at variance with the expectation due to the Navier-slip condition. Friction at the solid/liquid interface has to be enhanced for higher viscosity of the melt. From variation of the molecular weight we know that temperature can be assumed to be an indirect parameter in our system influencing slippage via the direct parameter viscosity. To conclude, we have presented a method to extract slip lengths from the analysis of rim profiles of dewetting polymer films. This method is a powerful tool to characterize slippage of dewetting liquid films. Further studies will focus on the variation of substrate and liquid properties. Viscoelastic properties of the liquid, i.e., high molecular-weight polymer chains above the entanglement length, may be topic of future research.

6 Acknowledgment

This work was financially supported by DFG grants JA 905/3 and MU 1626/5 within the priority program SPP 1164, the European Graduate School GRK 532 and the Graduate School 1276. We acknowledge the generous support of Si wafers from Siltronic AG, Burghausen, Germany.

References

1. Tretheway D C, Meinhart C D (2002) *Phys Fluids* 14:L9

2. Tretheway D C, Meinhart C D (2004) *Phys Fluids* 16:1509
3. Lumma D, Best A, Gansen A, Feuillebois F, Rädler J O, Vinogradova O I (2003) *Phys Rev E* 67:056313
4. Pit R, Hervet H, Leger L (2000) *Phys Rev Lett* 85:980
5. Schmatko T, Hervet H, Leger L (2005) *Phys Rev Lett* 94:244501
6. Craig V S J, Neto C, Williams D R M (2001) *Phys Rev Lett* 87:054504
7. Vinogradova O, Yakubov G E 2003 *Langmuir* 19:1227
8. Cottin-Bizonne C, Jurine S, Baudry J, Crassous J, Restagno F, Charlaix E (2002) *Eur Phys J E* 9:47
9. Zhu Y, Granick S (2002) *Langmuir* 18:10058
10. Neto C, Evans D R, Bonaccorso E, Butt H-J, Craig V S J (2005) *Rep Prog Phys* 68:2859
11. Lauga E, Brenner M, Stone H A (2005) *Handbook of Experimental Fluid Dynamics*. Springer, New York
12. Bocquet L, Barrat L (2007) *Soft Matter* 3:685
13. Ruckenstein E, Jain R K (1974) *J Chem Soc Faraday Trans II* 70:132
14. Seemann R, Herminghaus S, Jacobs K (2001) *Phys Rev Lett* 86:5534
15. Reiter G (1992) *Phys Rev Lett* 68:75
16. Seemann R, Herminghaus S, Jacobs K (2001) *Phys Rev Lett* 87:196101
17. Fetzer R, Münch A, Wagner B, Rauscher M, Jacobs K (2007) *Langmuir* 23:10559
18. Wassermann S R, Tao Y-T, Whitesides G M (1989) *Langmuir* 5:1074
19. Good R J, Girifalco L A (1960) *J Phys Chem* 64:561
20. Brochard-Wyart F, De Gennes P-G, Hervet H, Redon C (1994) *Langmuir* 10:1566
21. Münch A, Wagner B, Witelski T P (2005) *J Eng Math* 53:359
22. Fetzer R, Jacobs K, Münch A, Wagner B, Witelski T P (2005) *Phys Rev Lett* 95:127801
23. Fetzer R, Rauscher M, Münch A, Wagner B A, Jacobs K (2006) *Europhys Letters* 75:638
24. Fetzer R, Jacobs K (2007) *Langmuir* 23:11617
25. Migler K B, Hervet H, Leger L (1993) *Phys Rev Lett* 70:287
26. Hervet H, Leger L (2003) *C R Physique* 4:241
27. Leger L (2003) *J Phys: Cond Matt* 15:S19
28. Pastorino C, Binder K, Kreer T, Müller M (2006) *J Chem Phys* 124:064902
29. Magerl A Private communication
30. Cottin-Bizonne C, Barrat J-L, Boquet L, Charlaix E (2003) *Nature Materials* 2:237
31. Cho J J, Law B M, Rieutord F (2004) *Phys Rev Lett* 92:166102